

www.acsami.org Research Article

Condensed Layer Deposition of Nanoscopic TiO₂ Overlayers on High-Surface-Area Electrocatalysts

Daniela V. Fraga Alvarez, Zhexi Lin, Zixiao Shi, Amanda F. Baxter, Emily D. Wang, Dhruti Kuvar, Nafis Mahmud, Muftah H. El-Naas, Héctor D. Abruña, David A. Muller, and Daniel V. Esposito*



Cite This: ACS Appl. Mater. Interfaces 2024, 16, 25432–25444



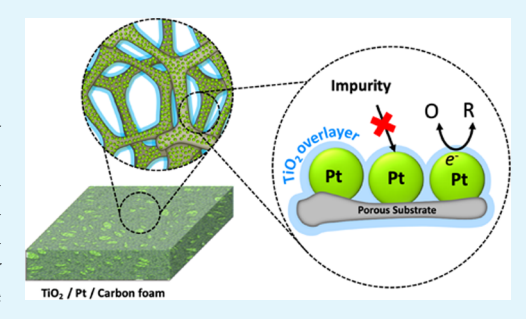
ACCESS I

Metrics & More

Article Recommendations

s Supporting Information

ABSTRACT: Encapsulating an electrocatalytic material with a semipermeable, nanoscopic oxide overlayer offers a promising approach to enhancing its stability, activity, and/or selectivity compared to an unencapsulated electrocatalyst. However, applying nanoscopic oxide encapsulation layers to high-surface-area electrodes such as nanoparticle-supported porous electrodes is a challenging task. This study demonstrates that the recently developed condensed layer deposition (CLD) method can be used for depositing nanoscopic (sub-10 nm thick) titanium dioxide (TiO_2) overlayers onto high-surface-area platinized carbon foam electrodes. Characterization of the overlayers by transmission electron microscopy (TEM) and electron energy loss spectroscopy (EELS) showed that the films are amorphous, while X-ray photoelectron spectroscopy confirmed that they exhibit



 TiO_2 stoichiometry. Electrodes were also characterized by hydrogen underpotential deposition (H_{upd}) and carbon monoxide (CO) stripping, demonstrating that the Pt electrocatalysts remain electrochemically active after encapsulation. Additionally, copper underpotential deposition (Cu_{upd}) measurements revealed that TiO_2 overlayers are effective at blocking Cu^{2+} from reaching the TiO_2 /Pt buried interface and were used to estimate that between 43 and 98% of Pt surface sites were encapsulated. Overall, this study shows that CLD is a promising approach for depositing nanoscopic protective overlayers on high-surface-area electrodes.

KEYWORDS: electrocatalysis, oxide overlayers, condensed layer deposition, buried interfaces, wet chemical synthesis, platinum, titanium oxide

I. INTRODUCTION

Electrocatalytic processes offer many promising avenues to harness electricity generated by renewable sources to decarbonize the chemical industry. However, improvements in the activity, selectivity, and stability of state-of-the-art electrocatalysts are necessary to make electrochemical processes more energy-efficient and economically competitive with today's fossil fuel-based chemical processes. Approaches for enhancing catalyst performance have included modifying the catalyst support, composition, structure, and loading. One emerging approach to improving electrocatalyst performance and long-term durability is applying ultrathin oxide coatings directly to the surface. See Within this oxideencapsulated electrocatalyst (OEC) architecture, electrocatalytic reactions can occur at the buried interface between the overlayer and encapsulated electrocatalyst if the overlayer is permeable to the reactant and product species. When properly designed, oxide overlayers can improve electrocatalyst stability, activity, and durability for a wide range of electrocatalytic reactions.^{9,10}

Many insights into the functionalities of semipermeable oxide encapsulation layers have been gained through studies of model thin-film electrodes for which the structure and composition of the oxide overlayer can be precisely

tuned.^{6,8,11} For example, thin-film Pt electrocatalysts encapsulated with ultrathin (2-10 nm) SiO_x (silicon oxide) overlayers were found to favor the oxygen evolution reaction (OER) over the chlorine evolution reaction (CER) in acidic and pHneutral seawater, relative to a bare Pt control. 10 These improvements have been ascribed to the SiO_x overlayer being selectively impermeable to Cl⁻ ions, thus preventing the CER at the buried Pt sites. Furthermore, SiO_x/Pt thin-film electrodes have also exhibited enhanced activity for the methanol oxidation reaction (MOR)⁷ and the ability to selectively permit the hydrogen evolution reaction (HER) while suppressing the $\rm O_2$ reduction reaction. ^{12,13} By varying the synthesis conditions of carbon-modified silicon oxide (SiO_xC_y) overlayers, Beatty et al. were able to show that the composition and structure of oxide overlayers can be tuned to control the relative fluxes of O₂ and H⁺ to electrocatalyst active sites thanks to the different transport mechanisms of O2 and

Received: December 7, 2023 Revised: March 27, 2024 Accepted: April 8, 2024 Published: April 30, 2024





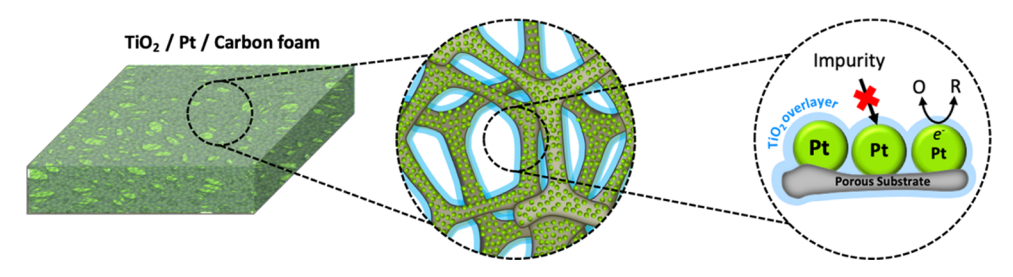


Figure 1. Rendering of titanium oxide (TiO₂)-coated platinized carbon foam (CF) electrodes, where the blue layer, green dots, and gray substrate represent the TiO2 overlayer, platinum nanoparticles, and porous carbon foam support material, respectively. The inset illustrates the basic operating process of the TiO₂/Pt/CF electrode.

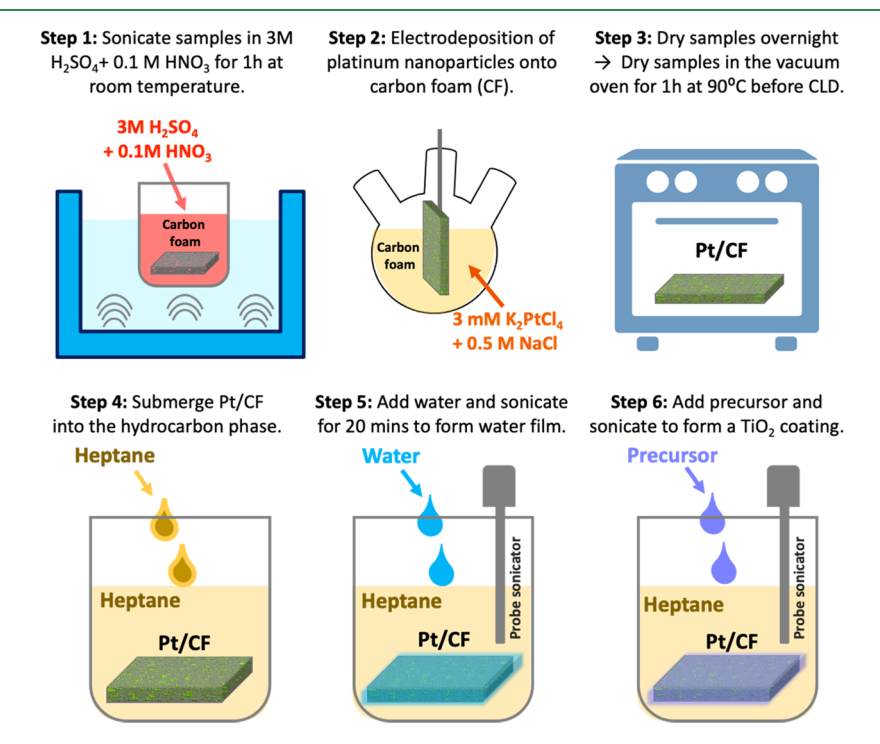


Figure 2. Key steps involved in the synthesis of TiO₂-encapsulated platinized carbon foam (Pt/CF) electrodes by CLD. This process was adapted from the CLD process described by Jasim et al.²⁴ Copyright 2020 nature communications materials.

H⁺ within the oxide. 11 Although these model thin-film electrodes are useful for correlating the thickness and composition of oxide overlayers with their transport properties and the OEC performance, high-surface-area porous electrodes are necessary for industrially relevant applications.

The first challenge of applying nanoscopic oxide coatings to porous electrodes is preparing conformal coatings on complex three-dimensional (3-D) structures. Atomic layer deposition (ALD) is one well-known method for depositing thin oxide layers on porous substrates, 14 but its application to porous electrodes faces several challenges, including inconsistent film growth rates on porous surfaces, limited choice of precursors, and relatively high cost. 15 Takenaka et al. demonstrated the application of uniform silica layers onto Pt nanoparticles supported on carbon nanotubes (CNTs) and Ketjen black (KB) by successive hydrolysis and polycondensation of 3aminopropyltriethoxysilane (APTES) and tetraethoxysilane (TEOS), as well as APTES and methyltriethoxysilane (MTEOS). 16-18 They achieved control over the diameter of the pores within the layers by incorporating $NH_2-(CH_2)_n$ NH_2 (n = 6, 8, and 10) during the synthesis process¹⁹ and enhanced stability, durability, and catalyst activity when the coated Pt/CNT and Pt/KB were tested in a polymer

electrolyte membrane fuel cell (PEMFC). 18-21 These methods, while effective, involve multiple steps, such as preparing the catalyst ink, which requires the addition of ionomers to enhance the adhesion of the coated particles onto the substrate. 22,23

A more streamlined approach would apply the oxide coating directly to catalyst-supported porous electrodes in a way that completely avoids the need for ionomers. One attractive method for achieving this structure is the recently developed condensed layer deposition (CLD) process, 24-28 which shares some similarities with sol-gel processes commonly used to make oxide nanoparticles and coatings. In the sol-gel synthesis of oxide materials, metal-organic precursors dissolved in a solvent undergo hydrolysis reactions to form a solution of colloidal particles, forming a biphasic gel that can be applied to a substrate to produce a coating. ^{29,30} In contrast, CLD avoids the formation of colloidal particles in the bulk solution by carrying out hydrolysis of the metal-organic precursor directly on the surface of the target substrate. This surface-confined hydrolysis process is enabled by forming a thin nanoscopic water film on the substrate surface before introducing the metal-organic precursor. This leads to dense, conformal oxide coatings while minimizing hydrolysis in the

bulk organic solvent. 24-27 Furthermore, Jasmin et al. showed that varying the thickness of the water film during the CLD process can be used to control the thickness of oxide layers deposited on nanoparticle substrates with nanometer-level precision.²⁴ In the current study, we extend the use of CLD to deposit nanoscopic titanium dioxide (TiO2) overlayers on high-surface-area platinum nanoparticle catalysts supported on monolithic porous carbon foam (CF) substrates (Figure 1). TiO₂ was chosen as the overlayer material for this study owing to its excellent chemical stability over a wide range of pH conditions,³¹ low toxicity,³² and previous successful uses of TiO₂ as the overlayer material in oxide-encapsulated electrocatalysts. 25,33,34

In contrast to previously reported uses of CLD, this study uses the CLD method to directly deposit oxide overlayers onto the entire electrode structure (catalyst + support) rather than isolated catalytic nanoparticles or support/binder material. A potential advantage of adopting this approach is that depositing the catalytic nanoparticle first ensures a satisfactory electrical contact between the catalyst and substrate, avoiding interfacial resistance that could arise between an oxideencapsulated electrocatalyst nanoparticle and a support material. As illustrated in Figure 2, this process consists of submerging a Pt/CF electrode into a nonpolar hydrophobic solvent (heptane) and adding water, which condenses on the surface of the electrode if the electrode is more hydrophilic than the solvent.²⁴ Next, a metal-organic precursor such as titanium(IV) ethoxide (TEO) is added to the reaction solution, where it hydrolyzes to form TiO2 when it contacts the water film on the surface of the electrode (eq 1). As the surface-confined water is the limiting reagent for the hydrolysis reaction, the thickness of the coating is determined by the thickness of the nanoscopic H₂O film on the substrate material. Based on this understanding, enhancing the hydrophilicity of the substrate by creating surface functional groups should result in a more uniform coating. ^{24–27} Xing et al. reported that sonicating carbon nanotubes in 3 M H₂SO₄ + 0.1 M HNO₃ at 60 °C for 2 h significantly increased the oxygen content on the surface of the nanotubes without major structural damage compared to samples treated for more extended periods.³⁵ Based on these observations, a surface functionalization step (Figure 2, Step 1) was applied in the current study to the CF substrate before Pt electrodeposition in order to make the surface of the carbon foam more favorable for the formation of a uniform water film during the CLD process. To prevent water from the surface functionalization and electrodeposition steps from affecting the subsequent CLD steps, samples were thoroughly dried overnight and in a vacuum oven at 90 °C for 1 h prior to the CLD process.

$$Ti(OC_2H_5)_4 + 2H_2O \rightarrow TiO_2 + 4C_2H_5OH$$
 (1)

Oxide overlayers deposited on porous electrodes via CLD can still exhibit nonuniformities, holes, or cracks. Such variations will likely give rise to different local selectivities, undesirable concentration overpotentials, and varying current densities across the electrode. Thus, this paper explores how varying the amounts of added precursor and water impacts the continuity and uniformity of the coating. First, physical characterization of the as-made high-surface-area carbon foam electrodes is presented based on the results of scanning electron microscopy (SEM), energy-dispersive X-ray spectroscopy (EDS), and selected area electron diffraction (SAED). A small subset of TiO₂-coated Pt thin films were also fabricated

to facilitate high-resolution characterization of the CLD coatings by X-ray photoelectron spectroscopy (XPS) measurements, electron energy loss spectroscopy (EELS), and transmission electron microscopy (TEM). The influence of the TiO2 coatings on the electrochemical properties of encapsulated Pt electrocatalysts was also probed by electroanalytical methods. Specifically, hydrogen underpotential deposition (H_{und}) and carbon monoxide stripping voltammetry were used to evaluate the electrochemically active surface area of encapsulated electrodes, while copper underpotential deposition (Cu_{upd}) measurements were used to assess the percentage of Pt sites covered by the TiO2 overlayer.

II. MATERIALS AND METHODS

II.I. Chemicals. Solutions were prepared using 18.2 $M\Omega$ ·cm deionized (DI) water, concentrated sulfuric acid (Certified ACS plus, Thermo Fisher Scientific), nitric acid (HNO3, Certified ACS plus, Fisher Chemical), sodium chloride (ACS Reagent grade, Sigma-Aldrich), potassium tetrachloroplatinate (99.99% trace metal basis, Sigma-Aldrich), and copper sulfate (CuSO₄, Sigma-Aldrich, Reagent-Plus), and purged with nitrogen gas (N2, Purity Plus 99.999% purity) and carbon monoxide (CO, Purity Plus 99.999% purity) as required by electrochemical experiments. The precursor for CLD was prepared with heptane (HPLC, ≥96% Fisher Chemical) and titanium(IV) ethoxide (TEO, technical grade, Sigma-Aldrich).

II.II. Electrode Fabrication. Electrodes were fabricated using porous conductive carbon foam (PCCF) characterized by 100 pores per inch (PPI) and sheet resistance of 7.82 \times 10⁻² Ω square⁻¹ (McMaster-Carr). The electrode was cut into a 1 cm \times 2.5 cm rectangle. The portion of the electrode tested was a rectangle of 1 cm × 1.5 cm with a thickness of 1.8 mm, while the portion of the electrode used as the electrical feedthrough remained at the original thickness of 5 mm. An electrical connection to the carbon foam was made by inserting a piece of titanium foil into a thicker segment of the electrode. See SI Section I, Figure S1. The planar silicon (Si) wafer electrodes were coated with 2 nm of Ti at 0.5 Å s⁻¹ followed by 50 nm of Pt (99.99%) at 1 Å s⁻¹ via electron-beam (e-beam) evaporation.

II.III. Electrodeposition of Platinum Nanoparticles. Electrodes were sonicated in isopropanol, methanol, and DI water for 5 min each to remove impurities from the surface. The electrodes were then submerged in a 3 M H₂SO₄ + 0.1 M HNO₃ solution and sonicated for 1 h at room temperature. The electrodes were rinsed thoroughly with DI water, and they underwent a two-step chronoamperometry (CA) procedure of 5 s each in a deaerated $0.5~M~H_2SO_4$ liquid electrolyte to further clean the surface of the electrode. The applied potential of the first CA step was 0.4 V vs Ag/AgCl, and the second CA was -0.8 V vs Ag/AgCl. Platinum nanoparticle electrocatalysts were deposited to the electrodes by carrying out cyclic voltammetry (CV) at 100 mV s⁻¹ in a 3 mM $K_2PtCl_4 + 0.5$ M NaCl electrolyte (pH = 2.60) for 21 cycles between -0.7 V vs Ag/AgCl and +0.3 V vs Ag/AgCl while stirring at 200 rpm.

II.IV. Electrochemical Surface Area. After electrodeposition, the electrochemical surface area of the electrodes was quantified by integrating the hydrogen underpotential adsorption and desorption features recorded during cyclic voltammetry (CV). Each electrode was cycled from 0.05 V vs RHE to 1.2 V vs RHE at 20 mV s⁻¹ in a three-neck round-bottom flask where a carbon rod was the counter electrode (CE) and Ag/AgCl was the reference electrode. The electrochemical surface area (ECSA) was calculated by integrating the hydrogen underpotential deposition (H_{upd}) signal, correcting for double-layer capacitance, and using the specific capacitance of H_{upd} on polycrystalline Pt of 210 μ C cm $_{Pt}^{-2.37,38}$ This procedure was repeated after coating and prior to electrochemical measurements to calculate the changes to ECSA resulting from the coating procedure.

II.V. Condensed Layer Deposition. Following electrodeposition and the electrochemical characterization, the samples were dried overnight for 12 h inside the fume hood. To further ensure that no

water from previous steps was present during CLD, the samples were dried in a vacuum oven for 1 h at 90 °C. The dried Pt/CF was submerged in 20 mL of heptane in a 60 mL Nalgene bottle. The total surface area of the porous electrode was calculated using its volume and the area/volume factor provided by the manufacturer for 100 PPI carbon foam of 2000 ft² ft^{-3,39} Brunauer-Emmett-Teller (BET) surface area measurements were also conducted using a Micromeritics ASAP 2020 adsorption analyzer with ultrahigh-purity N2 at a pressure range of P/P^0 between 0.05 and 0.30, where P is the equilibrium pressure and P^0 is the saturation pressure. The measured surface area was 0.406 ± 0.099 m² g⁻¹, which is in reasonable agreement with the value provided by the manufacturer. See ESI Section I for more details. The Nalgene bottle containing heptane + water was mounted inside the fume hood, and the probe sonicator (QEX 750) was introduced through a hole (diameter, 0.7 cm) that was drilled on the lid. To prevent moisture from reaching the sample, a plastic pipet was introduced to continuously purge the headspace with N2 through a small hole punctured on the side of the bottle. The samples in the heptane + water mixture were sonicated for 20 min at an amplitude of 27% and on-and-off pulses of 5 and 1 s, respectively. Once the first sonication step was finished, a stoichiometric amount of ~0.2 M titanium(IV) ethoxide in heptane solution was added using a syringe. Due to the high volatility of heptane, the evaporated solvent in the bottle was replenished before the second sonication step. The samples in heptane + water + TEO solution were sonicated for 10 min under identical conditions as the first step. Finally, the samples were carefully removed, placed in a glass Petri dish, and dried overnight inside a fume hood. Dried samples were stored in separate vials. In the case of planar samples, the surface activation process was skipped to avoid harming the Pt and Ti layers during a harsh acidic sonication bath. The preparation steps for these samples were the same as those for the porous samples. To increase the total surface area, a dummy carbon foam measuring 1 cm × 1 cm × 0.5 cm was introduced into the Nalgene bottle to increase reagent quantities to larger and, therefore, more workable volumes.

II.VI. Materials Characterization. Scanning electron microscopy (SEM) images and energy-dispersive X-ray spectroscopy (EDX) elemental maps were obtained by using a Zeiss Gemini 500 instrument and a Zeiss Sigma VOP microscope. Accelerating voltages ranged from 5 to 12 kV. EDS maps were used to obtain the platinum and titanium distribution as a function of cross-sectional position, which was generated by slicing the Pt and Ti EDS maps into 10 bins horizontally, counting the pixel intensity in each bin, and normalized to those of the corresponding carbon EDS map pixel intensities. EDX elemental mapping and selected area electron diffraction (SAED) pattern on corresponding TiO₂ encapsulated carbon form were collected with an FEI TALOS F200X transmission/scanning transmission electron microscope (S/TEM) equipped with a highangle annular dark-field (HAADF) detector and a CCD camera at 200 kV. TiO2-coated platinum thin films deposited on silicon wafers were cross-sectioned and prepared using Thermo Fisher Helios G4 UX Focused Ion Beam milling by applying a protective layer of carbon using a Sharpie pen, followed by the deposition of a platinum (Pt) layer through ion beam deposition, see ESI Figure S2. Scanning transmission electron microscopy (STEM) measurements were performed using Thermo Fisher FEI Spectra 300 TEM with ultrahigh-brightness cold field emission gun (C-FEG) and spherical aberration correction ("Kraken" at Cornell University). The STEM resolution was 58 pm with probe current at 75 pA and 300 kV. The high-angle annular dark-field (HAADF) image was collected with a C₂ aperture of 70 μ m, camera length of 94 mm, and convergence angle of 30 mrad. The HAADF image stacks were taken with 2048 × 2048 pixels with a 5 μ s dwell time. The EELS data were recorded by using a Continuum CMOS camera with an energy dispersion of 0.3 eV per channel. Cornell Spectrum imaging tool was used to process the EELS data from images. 40 X-ray photoelectron spectroscopy measurements were conducted in a PHI-5600 spectrometer with an Al-K α X-ray source. The scan rate was 0.05 eV s⁻¹ with a pass energy of 23 eV. Ti 2p, O 1s, and Pt 4f spectra were calibrated with metallic Pt 4f_{7/2} at 71.1 eV. 11,41 The peak deconvolution was performed by identifying the Ti 2p and O 1s peaks associated with ${\rm TiO_2}^{42}$ and surface oxygen species. 43

II.VII. Electrochemical Measurements. All electrochemical measurements were conducted using a SP-200 BioLogic potentiostat. All standard three-electrode measurements used a carbon rod (Saturn Industries) counter electrode (CE), a AglAgCl (E° = 0.21 V vs NHE, Hach, E21M002) reference electrode, and Pt/CF or TiO2/Pt/CF as the working electrode. Solutions were deaerated with nitrogen (N₂, Purity Plus 99.999% purity) at 1 atm pressure, and the pH was measured using a benchtop pH meter (Fisherbrand accumet AE150 Benchtop pH Meter) that was calibrated using pH buffers of 1.68, 4.01, and 7.0. Prior to carbon monoxide (CO) oxidation experiments, each electrode was cycled from 0.01 V vs RHE to 1.2 V vs RHE at 20 mV s⁻¹ in 0.5 M H₂SO₄ for 5 cycles in a three-neck round-bottom flask. Next, the background signal was recorded in deaerated 0.5 M H₂SO₄ during cyclic voltammetry (CV) for 3 cycles at 20 mV sec⁻¹ from 0.4 V vs RHE to 0.01 V vs RHE to 1.2 V vs RHE. CO was then adsorbed to the surface of the electrode by saturating the electrolyte with CO_(g) for 10 min at 400 rpm while holding the electrode at a potential of 0.05 V vs RHE. The excess CO was removed by purging the headspace of the three-neck flask with N2 for 10 min while stirring the electrolyte with a magnetic stir bar (set to 400 rpm) and maintaining an applied potential of 0.05 V vs RHE. To "strip" the CO, the stirring was stopped, and a CV scan from 0.4 V vs RHE to 0.01 V vs RHE to 1.2 V vs RHE at 20 mV s⁻¹ was applied. To ensure that all CO was removed from the surface of the electrode, 2 additional CVs under equal conditions were conducted. To quantify the ECSA of platinum particles where CO was adsorbed, the difference between the integrated charge passed by the first and third CV was calculated and converted using the known factor of 420 μ C cm_{Pt}^{-2.4}

Copper stripping experiments were performed in a well-stirred (200 rpm) three-neck flask in deaerated 0.5 M H₂SO₄. Prior to copper stripping experiments, each electrode was cycled from 0.05 V vs RHE to 1.2 V vs RHE at 20 mV s⁻¹ in 0.5 M H₂SO₄ for 5 cycles in a threeneck round-bottom flask. The background signal was measured via linear sweep voltammetry (LSV) from 0.38 V vs RHE to 1.00 V vs RHE at 20 mV s⁻¹. Following the first LSV, 2 mM copper sulfate (CuSO₄) was added to the 0.5 M H₂SO₄ supporting electrolyte contained in the three-neck flask. The 0.5 M H₂SO₄ + 2 mM CuSO₄ solution was stirred thoroughly and purged with $N_{2^{\prime}}$ and the pH was measured before reintroducing the working electrode. Three consecutive measurements were carried out, starting with an LSV from 0.38 V vs RHE to 1.00 V vs RHE at 20 mV s⁻¹, followed by a chronoamperometry (CA) at 0.38 V vs RHE for 5 min, and a final LSV from 0.38 V vs RHE to 1.00 V vs RHE at 20 mV s⁻¹. The background signal was subtracted from the copper stripping LSV, and the amount of Pt nanoparticles where Cu²⁺ ions were deposited was quantified by integrating the Cu_{upd} signal and using the conversion factor of 420 μ C cm_{Pt}⁻².

III. RESULTS AND DISCUSSION

III.I. Physical Characterization. TiO₂/Pt/CF samples were prepared by CLD as described in Sections I and II. Briefly, samples with varying amounts of TiO2 were fabricated by adding varying quantities of water (3.4, 4.90, and 9.8 μ L) to the reaction vessel, followed by the addition of TEO to trigger the TiO2-forming hydrolysis reaction shown in eq 1. To promote the complete conversion of water to TiO₂, 10% excess TEO was added compared to the stoichiometric amount required according to eq 1 ($H_2O/TEO = 2:1$). Vertical sonication was used to assist the dispersion of the added water and TEO throughout the sample. It is important to note that sonication/deposition time may also impact the uniformity of the coating, especially for porous material with relatively low porosity, which might require longer times than the conditions used in this study. Throughout this paper, samples are labeled as "low", "medium", and "high", to refer to the relative quantity of H₂O used during the CLD process. Based on previous

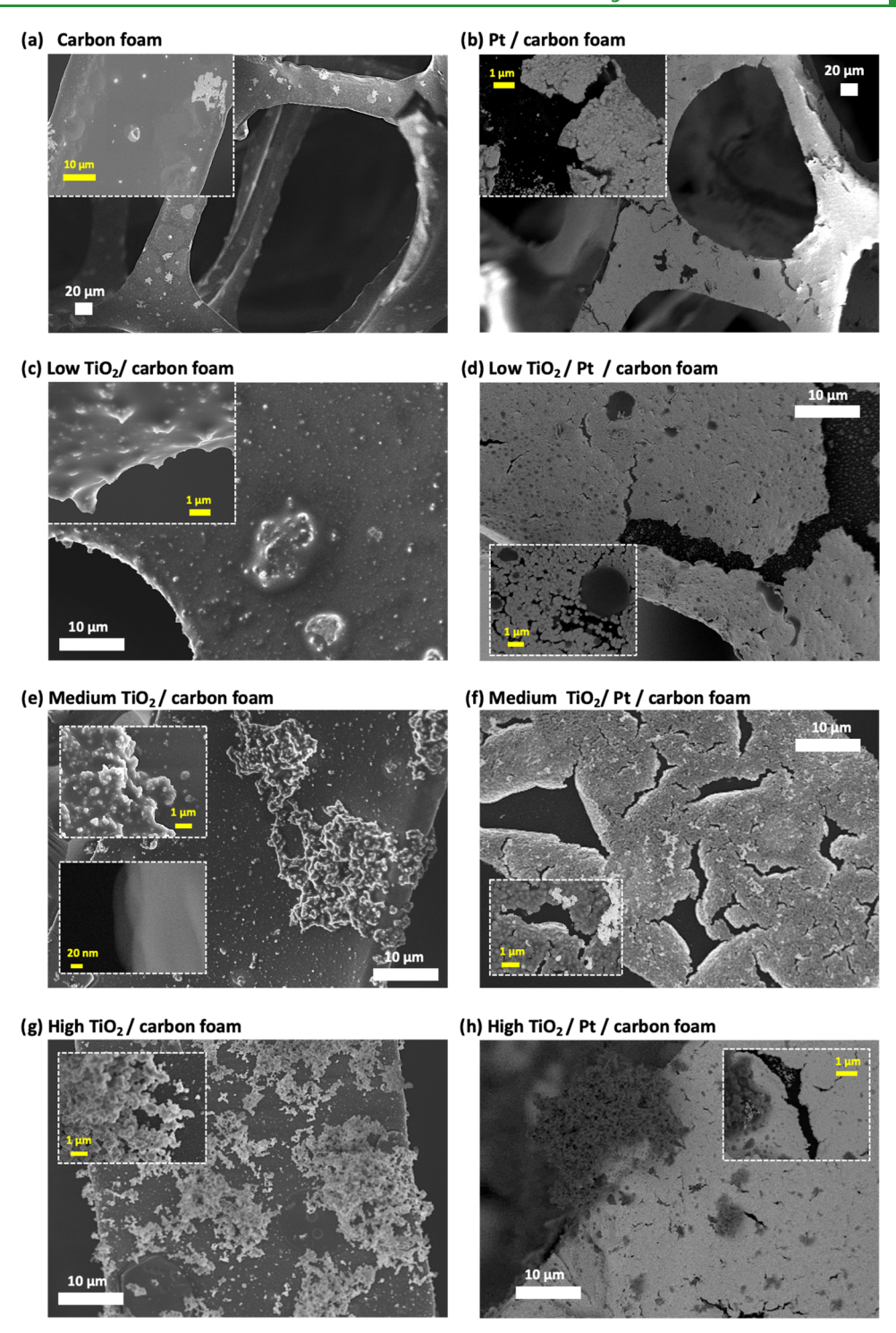


Figure 3. SEM images of coated and uncoated carbon foam and Pt/carbon foam. The images show (a) uncoated carbon foam, (b) Pt/coated carbon foam (Pt/CF), and carbon foam with (c) "low", (e)" medium", and (g) "high" water concentrations used during CLD. Additionally, (d, f, h) show the corresponding Pt/carbon foam samples with the same water concentrations used during the CLD process.

studies employing CLD on nanoparticle substrates, 24 increasing the amount of H_2O relative to the surface area of the substrate leads to thicker TiO_2 coatings.

Substrate materials and TiO₂-encapsulated electrodes were first characterized by SEM, with representative images provided in Figure 3 for surface functionalized bare carbon foam (Figure 3a), platinized carbon foam (Figure 3b), TiO₂-encapsulated carbon foam (Figure 3c,e,g), and TiO₂-coated platinized carbon foam (Figure 3d,f,h). As seen in Figure 3a,

the carbon foam substrate consists of 50 to 90 μ m thick interconnected strands of carbon that form pores having diameters varying between 200 and 300 μ m. In Figure 3b, the electrodeposited platinum formed a layer that covered a large percentage of the surface of the carbon foam, although clear gaps in the Pt layer are evident. Higher resolution SEM images (SI Section III, Figure S3) showed that the light-colored Pt deposits formed ~200 nm particles that are often connected to neighboring particles, forming a semicontinuous network. After

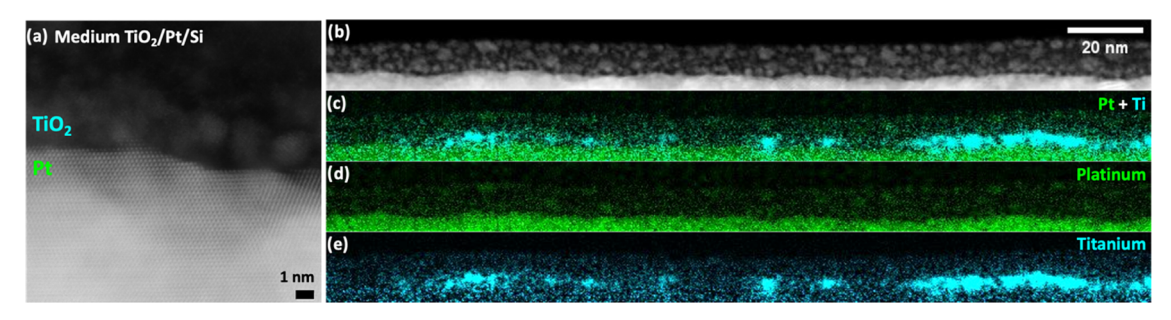


Figure 4. Dark-field TEM images of $TiO_2/Pt/Si$ wafer samples for which the TiO_2 coating was deposited under a "medium" water concentration during CLD (a, b). EELS elemental mapping shows the (c) Pt (green) + Ti (light blue), (d) Pt (green), and (e) Ti (light blue) distribution on the sample. See SI Section III, Figure S8 for extended EELS elemental mapping, including carbon and oxygen.

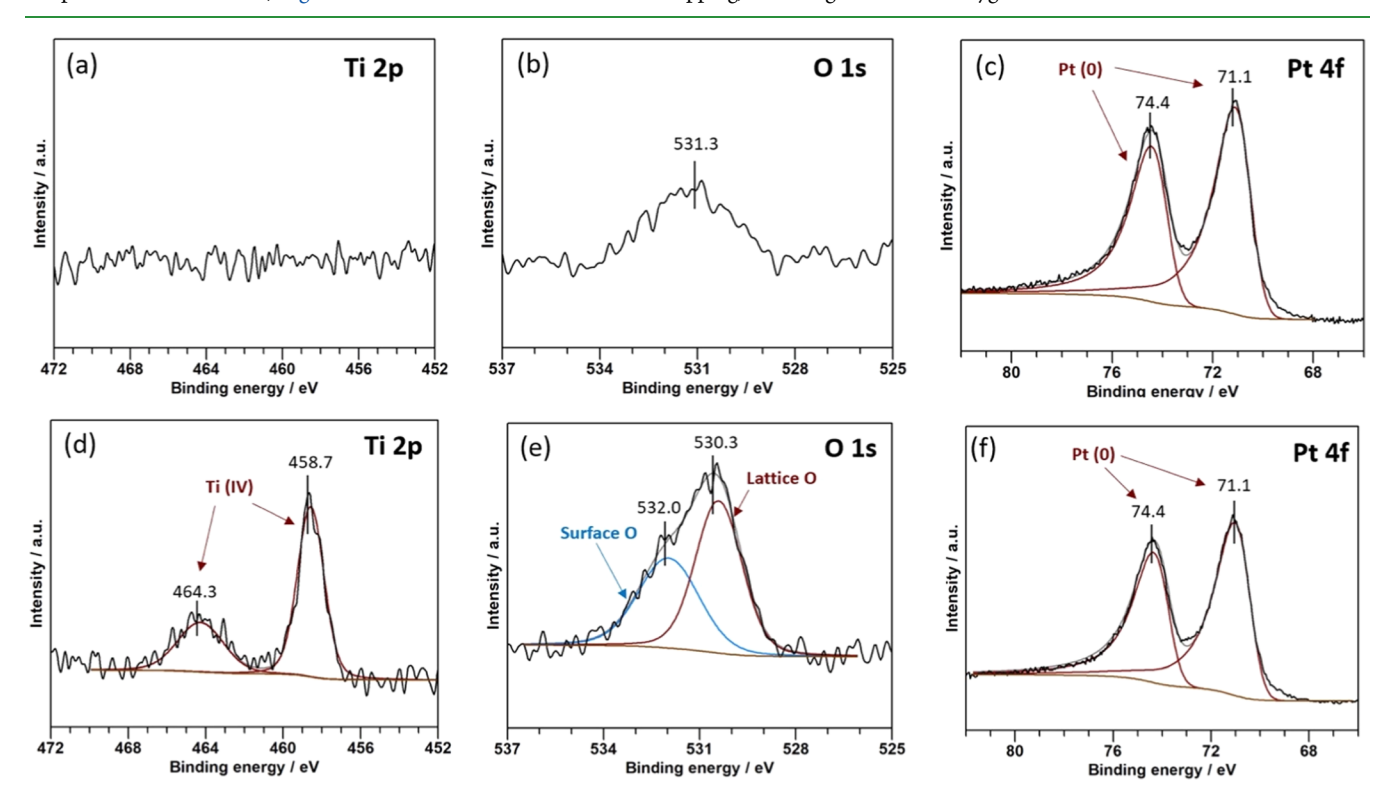


Figure 5. XPS characterization of the thin-film electrodes. (a) Ti 2p, (b) O 1s, and (c) Pt 4f spectra of the bare Pt/Si electrode; (d) Ti 2p, (e) O 1s, and (f) Pt 4f spectra of a TiO₂-encapsulated Pt/Si electrode fabricated using the "medium" water concentration during the CLD process. The y-axis ranges for the Ti 2p, O 1s, and Pt 4f spectra were kept the same between the two electrodes for easy comparison.

the ${\rm TiO_2}$ coating was applied to the bare carbon foam, splotchy deposits appeared on its surface (Figure 3c,e,g). These features are most evident when the CLD process is carried out using the "high" water concentration (Figure 3g). When the CLD process was applied to the platinized samples, there was no noticeable difference in morphology between the uncoated (Figure 3b) and coated Pt/CF (Figure 3d,f,h). Energydispersive X-ray spectroscopy (EDS) images of "medium" TiO₂/Pt/CF samples (SI Section III, Figures S4 and S5) reveal a relatively uniform distribution of platinum and titanium signals spanning the cross-section of the platinized coated electrode. The unevenness of the carbon foam shown in the cross-sectional sample (Figure S5) is due to the freeze-cracking method used to preserve the TiO₂ overlayer. Although the Ti signal was relatively low due to the thin layer of TiO₂ (Figure S5f), the EDS spectra provided in Figure S5g confirm the presence of Ti. The EDS maps were analyzed as described in the Section II to obtain the Pt and Ti distributions as a function of cross-sectional position (Figure S5c).

To better characterize the nanostructure and chemical composition of the TiO₂ coatings, the coating process was also carried out under "medium" water concentration during CLD conditions to deposit TiO2 onto smooth, 50 nm thick, platinum thin films supported on 2 nm Ti + Si(100) substrate. In Figure 4a, a cross-sectional high-angle annular dark-field (HAADF) image from the "medium" TiO₂/Pt/Si wafer confirms that the TiO2 forms an overlayer on the Pt surface and indicates that the TiO2 coating has a highly disordered structure, in contrast to the adjacent Pt layer. This was confirmed with selected area electron diffraction (SAED, SI Section III, Figure S6), which does not show a discernible diffraction pattern associated with crystalline TiO2, indicating that the TiO₂ is disordered/amorphous. 45,46 EELS elemental maps captured on a different location of the same sample (Figure 4c-e) showed that the TiO₂ layer had a thickness that ranged between <1 and 5 nm. Consistent with the literature for thin TiO_2 layers, $Ti-L_{2,3}$ edges seen in the EELS spectra (SI Section III, Figure S7)⁴⁰ were detected at approximately 455

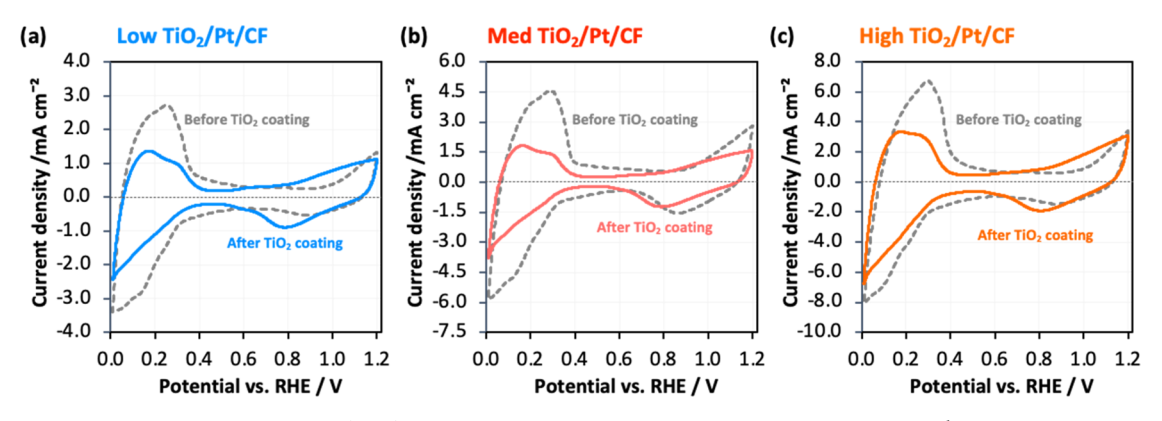


Figure 6. Hydrogen underpotential deposition (H_{upd}) cyclic voltammetry measurements carried out at 20 mV s⁻¹ from 0.05 V vs RHE to 1.2 V vs RHE in deaerated 0.5 M H₂SO₄ before (dashed lines) and after (solid lines) coating each Pt/CF electrode with TiO₂ using (a) "low", (b) "medium", and (c) "high" water concentrations during CLD. The 3rd CV cycle out of three total CV cycles is shown for "before TiO2 coating" (dashed lines), and the 3rd CV cycle out of five total CVs for "after TiO2 coating" (solid lines) for each electrode.

eV, while the O-K edge appeared at 553 eV.⁴⁷ The single K-O edge is further evidence of the disordered nature of the TiO₂ overlayer.

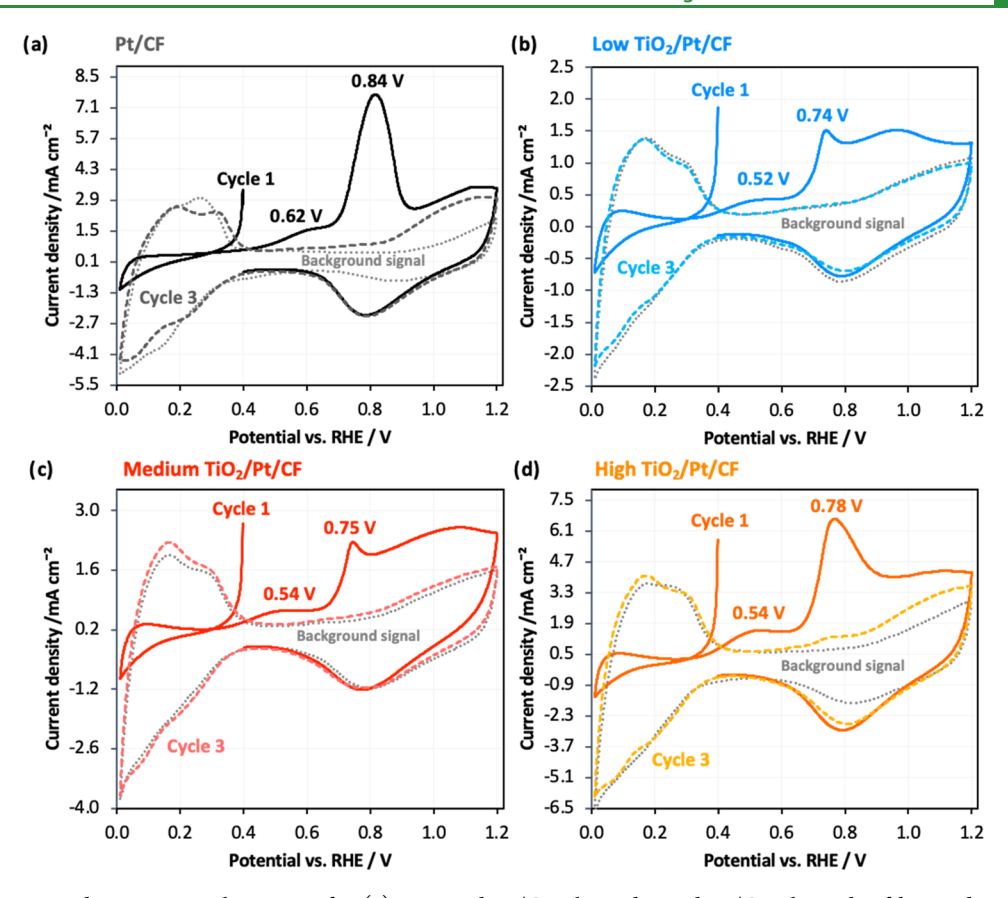
X-ray photoelectron spectra of a "medium" TiO₂/Pt/Si sample are compared to a bare Pt/Si control in Figure 5. For the bare Pt control sample, the peak center binding energies in the Pt 4f spectra (Figure 5c) are consistent with the Pt thin film being present in the metallic Pt state (Pt⁰), while the minor O 1s signal appearing around 531.3 eV in Figure 5b can be attributed to adventitious oxygen species such as surface hydroxyls and adsorbed CO₂. 43 XPS results for the TiO₂/Pt/Si sample are shown in Figure 5d–f. In Figure 5d, the Ti $2p_{1/2}$ and Ti 2p_{3/2} peak center binding energies of 464.3 and 458.7 eV are consistent with TiO₂, ⁴⁸ which is further supported by finding a Ti/O ratio of 0.47 using the Ti 2p peak area and the lattice oxygen peak area at (530.3 eV) (SI Section SIV, Table S1). Oxygen species located at higher binding energy (\approx 532 eV) were deconvoluted from the lattice oxygen and included hydroxyl species, water, and adsorbed CO₂. Comparing the Pt 4f peaks of the bare Pt and TiO₂-encapsulated samples (Figure 5c,f), the Pt 4f peak locations are the same, but the intensity of the Pt 4f peak for the TiO₂/Pt/Si sample is attenuated by 16% due to screening of photoelectrons by the TiO₂ overlayer. The Pt 4f and Ti 2p peak areas were also used as inputs to an overlayer calculation (SI Section SIV and eq S4), which was used to estimate a TiO2 overlayer thickness of 6.5 nm for the "medium" TiO2/Pt/Si sample. This estimate is consistent with the observations from the TEM images and EELS maps in Figure 4. Overall, XPS results provided evidence that an ultrathin TiO₂ encapsulation layer was successfully applied over a metallic Pt/Si substrate.

III.II. Electrochemically Active Surface Area (ECSA). The electrochemical surface area (ECSA) of Pt-based electrodes is commonly determined via hydrogen underpotential deposition (H_{upd}) measurements, whereby the charge associated with the adsorption and desorption of a monolayer of hydrogen is used to quantify the total number of active sites.³⁸ Many studies have shown that cyclic voltammetry profiles for polycrystalline Pt from 0.05 V vs RHE to 1.4 V vs RHE show well-defined features of electro-adsorption and electro-desorption of H_{upd} as well as PtO_x formation and reduction.^{38,49} When polycrystalline Pt electrodes are tested in sulfuric acid solutions, H_{upd} features are typically observed between 0.05 V vs RHE to 0.35 V vs RHE, while the signal associated with double-layer capacitance dominates the CV

profile from 0.40 V vs RHE to 0.85 V vs RHE. At more positive potentials, features associated with Pt oxidation (PtO_x) are seen in the positive scan, and features associated with the reduction of those species are seen during the reverse scan. 38,49 As seen in Figure 6, CV curves for all bare Pt (gray dash lines) and TiO₂-encapsulated Pt/CF (solid lines) samples exhibit features associated with H_{upd} and PtO_x that are characteristic of polycrystalline Pt electrodes. 38,49 The ECSA of the bare Pt/CF and low, medium, and high TiO2/Pt/CF electrodes were calculated by integrating the H_{upd} area, corrected for double-layer capacitance, and using the specific capacitance of H_{upd} on polycrystalline Pt of 210 μ C cm_{Pt}^{-2,38} The normalized ECSA for which the electrochemically active surface area has been normalized by the geometric surface area, also known as area per area factor, ranged from 55.7 to 270.7 $cm_{geo}^2 cm_{Pt}^{-2}$.

The presence of notable H_{upd} features for all TiO₂/Pt/CF electrodes indicates that protons were able to travel through the TiO₂ overlayer and reach the buried TiO₂/Pt interface. Nonetheless, the decrease in the magnitude of the H_{upd} features observed in the CVs after TiO2 coating (solid lines) indicates some loss in electrochemical surface area (Figure 6). Coated samples exhibited an average of $46 \pm 12\%$ decrease in H_{upd}-derived ECSA. Possible explanations include detachment of some platinum nanoparticles from the support during CLD or blocked active sites caused by regions of the electrode that are encapsulated by thicker coatings or particulate deposits (SI Section SV, Figure S9), which could significantly suppress the ability of the buried interface in these regions to access H⁺ and be in ionic communication with the electrolyte.

Besides affecting the H_{upd} signal, the addition of the CLD TiO₂ coating significantly alters the Pt oxidation redox features in the CV profiles of Figure 6. Most notably, the presence of the TiO₂ coating is observed to shift the onset for Pt oxidation between -200 and -230 mV compared to that observed for bare Pt, which is seen to be around 0.85 V vs RHE as expected. Additionally, increasing the water concentration during the CLD process resulted in a slightly smaller shift in the PtO_x onset potential. Previous work has claimed that negative shifts in the Pt oxidation onset potential can be caused by the ability of the overlayer to suppress sulfate adsorption, which competes with the formation of Pt-OH by blocking the adsorption of H_2O molecules. $^{7,50-52}$ Assuming that this explanation applies to the TiO2/Pt electrodes studied here, the observed shifts in the PtO_x redox features provide further evidence that most of



www.acsami.org

Figure 7. Carbon monoxide stripping voltammetry for (a) uncoated Pt/CF electrodes and Pt/CF electrodes fabricated using (b) "low", (c) "medium", and (d) "high" water concentrations during the CLD coating process. All CVs were conducted in deaerated 0.5 M H_2SO_4 at 20 mV s⁻¹ from 0.4 V vs RHE to 0.01 V vs RHE to 1.2 V vs RHE. Background CV in CO-free 0.5 M H_2SO_4 (gray dotted lines) were recorded before carrying out three successive CVs for the CO-poisoned electrode, where cycle 1 (solid lines) and cycle 3 (dashed lines) have been included in this figure.

the Pt nanoparticles are successfully encapsulated by the ${\rm TiO_2}$ layer.

The ECSAs of bare Pt and TiO_2/Pt electrodes were also measured by carbon monoxide (CO) stripping voltammetry, a technique that closely resembles $H_{\rm upd}$ but instead uses the oxidation of monolayer levels of adsorbed CO to probe the number of active sites on the sample surface. As CO is also known as a catalyst poison in direct methanol fuel cells (DMFC), the location (i.e., peak potentials) of CO oxidation features recorded during CO stripping is also used to probe the tolerance of an electrocatalyst to this poison. CO oxidation occurs on Pt through a Langmuir—Hinshelwood reaction mechanism that involves a reaction between adsorbed CO (eq 3) and adsorbed hydroxyls, the latter of which is formed electrochemically as shown in eq 2.54,55

$$H_2O + Pt \rightarrow Pt - OH_{ads} + H^+ + e^-$$
 (2)

$$Pt - CO_{ads} + Pt - OH_{ads} \rightarrow CO_2 + H^+ + e^- + 2Pt$$
 (3)

In this work, CO was first adsorbed onto the surface of the electrode while purging the solution with CO and holding the potential at 0.05 V vs RHE for 10 min. After removing dissolved CO from the bulk solution by purging with N_2 gas, the CO was "stripped" from the surface by sweeping the potential to positive (oxidizing) potentials. ^{56,57}

CO stripping voltammetry was performed on three different TiO₂-encapsulated Pt/CF electrodes and a bare Pt/CF control sample. Cyclic voltammetry scans recorded before stripping (dotted gray lines), immediately after stripping (cycle 1, solid

lines), and after 2 scans (cycle 3, dashed lines) are presented in Figure 7. The bare Pt/CF sample exhibited a small shoulder at 0.62 V vs RHE and a peak at 0.83 V vs RHE (Figure 7a). H_{upd} features were observed during the third scan, indicating that all of the CO was "stripped" from the electrode surface, allowing H^+ to adsorb onto the Pt. A larger peak for PtO_x was observed around 0.85 V vs RHE after the CO was "stripped" from the surface compared to the background CV, which was conducted in deaerated 0.5 M H_2SO_4 before all electrochemical measurements. The CO oxidation peak centers recorded for the $TiO_2/Pt/CF$ electrodes (0.74–0.78 V vs RHE) were all lower than that recorded for the bare Pt/CF control sample (0.84 V vs RHE). A prepeak located \approx 200 mV less positive than the primary CO oxidation peak was also observed for all coated samples.

The locations of the CO oxidation peak and onset potentials observed for the bare Pt/CF sample are consistent with reported literature values. The less positive onset and peak potentials for CO oxidation recorded for the low, medium, and high $\text{TiO}_2/\text{Pt/CF}$ have also been observed in other studies for SiO_x -coated and TiO_2 -supported Pt electrocatalysts. Some of the possible explanations for this phenomena include: (i) an increased presence of more reactive lattice oxygen in the TiO_2 overlayer promotes CO oxidation, which is hydroxyl groups (e.g., silanols in SiO_x) present in the overlayer may help facilitate CO removal at lower overpotentials than required for Pt-OH-facilitated CO removal (eq 3), and (iii) strong interactions between Pt atoms bonded to Ti atoms in TiO_2 , which can lower the activation energy for CO to adsorb onto

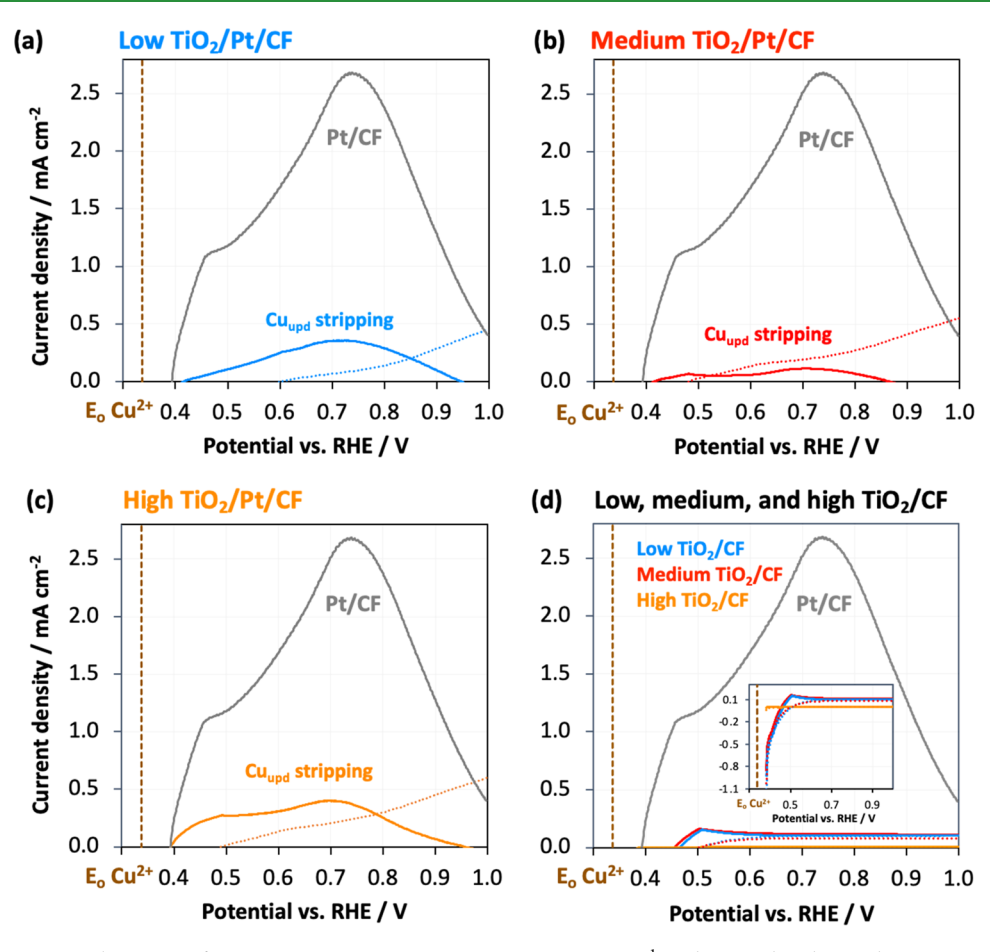


Figure 8. Copper stripping voltammetry from 0.38 V vs RHE to 1 V vs RHE at 20 mV s⁻¹ in deaerated and stirred 0.5 M H₂SO₄ + 2 mM CuSO₄ for (a) "low", (b) "medium", and (c) "high" TiO2/Pt/CF as well as (d) low, medium, and high TiO2/CF. Gray solid lines and dotted LSVs indicate bare Pt/CF Cu²⁺ stripping and background signal in deaerated 0.5 M H₂SO₄, respectively. Background LSV (dotted lines) was subtracted from all Cu_{upd} LSVs (solid lines).

the surface and can facilitate its diffusion. 63,64 Regardless of the exact mechanism, the less positive onset and peak potentials for CO oxidation can most likely be attributed to the presence of the TiO2 overlayer and the microenvironment it creates at the TiO₂/Pt buried interface.

The lower CO oxidation onset potential for the encapsulated samples also suggests that the TiO₂ overlayer alters the energetics associated with binding of CO to active sites at the buried interface compared to Pt atoms exposed to the bulk electrolyte. For example, steric influences associated with a nanoconfined environment at the buried interface might alter how the CO molecule coordinates with the Pt, which can change in orientation and impact its binding energy. Furthermore, the overlayer might alter the local electric field by changing the distribution of supporting electrolyte charges near the adsorbed CO molecules. Overall, the presence and nature of the CO stripping signal indicate that the CO molecules can penetrate through the TiO2 overlayer and be oxidized at active sites at the buried interface.

III.III. Cu Stripping Voltammetry. A second underdeposition method, copper stripping voltammetry, was also used to assess the ECSA and further quantify the coverage of Pt by the TiO₂ overlayers. As shown in eq 4, copper stripping is based on the underpotential deposition of Cu2+ ions onto the Pt surface. The adsorbed underpotentially deposited Cu atoms (Cu_{upd}) are subsequently oxidized or "stripped" from the Pt nanoparticles by sweeping to more positive potentials.

However, previous work has shown that dense oxide encapsulation layers are highly effective at blocking the relatively large solvated Cu2+ ions from reaching the oxide/ Pt interface.⁸ Thus, for overlayers that completely block the transport of Cu²⁺ to the buried interface, the suppression in the Cu_{und} signal by encapsulated electrodes compared to bare Pt controls can be used to estimate the percentage of Pt active sites that remain exposed to the bulk electrolyte due to cracks, holes, or partial delamination of the oxide layer. This quantification is carried out by integrating the Cu_{upd} signal and using the known conversion factor of 420 μ C cm⁻² Pt for polycrystalline Pt.44

$$Cu^{2+} + 2e^{-} \leftrightharpoons Cu_{upd} \tag{4}$$

Cu stripping voltammetry measurements were carried out for bare Pt/CF and TiO₂/Pt/CF electrodes made with "low", "medium", and "high" water concentrations during the CLD process. First, the background signal for all samples was measured by carrying out linear swept voltammetry (LSV) from 0.38 V vs RHE to 1.00 V vs RHE at 20 mV s⁻¹ in the Cufree supporting electrolyte. After adding 2 mM copper sulfate to the supporting electrolyte, the electrode was held at an (under)potential of 0.38 V vs RHE for 5 min to allow Cu²⁺ ions to adsorb onto exposed Pt sites. Immediately after, the Cu_{und} ions were oxidized by sweeping the potential to 1.0 V vs

RHE at 20 mV s⁻¹. Both the background and Cu stripping LSV curves are shown in Figure 8.

In Figure 8, the copper stripping voltammetry curve for the bare Pt/CF electrode exhibits a distinct oxidation peak centered at \approx 0.74 V vs RHE and a shoulder at \approx 0.46 V vs RHE, which is similar to the results obtained in other studies for polycrystalline Pt. 6,65,66 In contrast, the TiO2/Pt/CF electrodes show broad, shallow peaks in the backgroundsubtracted Cu stripping curves (Figure 8a-c), while the TiO₂coated CF control samples (Figure 8d) do not display any peaks. The negligible shift in Cu_{upd} oxidation peak potentials for the TiO₂/Pt/CF electrodes indicates similar binding energies to the bare Pt control sample, suggesting that the Cu_{upd} signal is observed due to cracks and holes that expose Pt nanoparticles and not due to Cu_{upd} stripped from the TiO₂/Pt buried interface. It was also observed that varying the water concentration during the CLD process, which in theory should result in different coating thicknesses, did not impact the transport of Cu²⁺ ions. This observation suggests that a similar TiO2 coverage of Pt was observed for low, medium, and high TiO₂/Pt/CF. Lastly, the inset in Figure 8d shows a significant reduction current for the low and medium TiO2/CF samples, possibly due to proton intercalation into the TiO₂ coating.

To summarize the results from H_{upd}, CO stripping, and Cu stripping measurements, ECSAs obtained from each electroanalytical method were plotted in Figure 9. In this figure, the

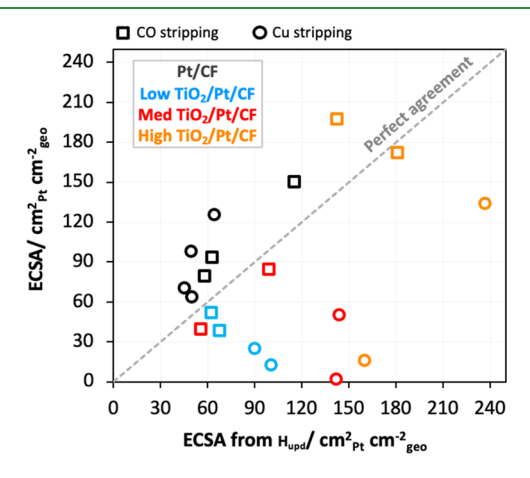


Figure 9. ECSAs measured from Cu_{upd} (circles) and CO oxidation (squares) signal as a function of area per area factor from the $H_{\rm upd}$ signal. Area per area factor for the low (blue), medium (red), and high (orange) TiO₂/Pt/CF samples as a function of H_{upd}. The dashed line represents the perfect agreement of area per area factors measured from Cu_{upd} or CO oxidation and H_{upd}.

ECSAs (i.e., cm² of active Pt) were normalized to the geometric area of the electrode, and the CO stripping and Cu stripping ECSAs were plotted vs the H_{upd} ECSA. Important insights may be gained based on the location of experimental data points with respect to the dashed gray line, which represents perfect agreement in the CO stripping or Cu stripping-determined ECSA and the H_{upd}-determined ECSA. Focusing first on the data points for the bare Pt/CF electrode, ECSAs determined by Cu and CO stripping overestimate H_{upd}-derived ECSA by 27-95%, and 31-49%, respectively. Previous studies have also reported that the Cu and CO stripping methods overestimate the electrochemical surface area of bare Pt samples compared to H_{upd} methods, possibly due to uncertainties associated with capacitance charge correction or the selection of the lower potential limit.⁶⁸ However, the Cu and CO stripping-derived ECSAs for the TiO₂/Pt/CF electrodes were 43-98%, and 5-43% lower, respectively, than the H_{upd}-derived ECSAs. Only one TiO₂/Pt sample tested exhibited a CO stripping-derived ECSA larger than its H_{und}-derived ECSA. While the differences between the CO stripping and H_{upd} ECSAs are quite small, the significant discrepancy between the Cu stripping and H_{upd} measurements can be attributed to the suppressed transport of Cu²⁺ through TiO₂ coatings to reach the buried interface. If it is assumed that the TiO₂ coatings are completely impervious to Cu²⁺ and all Cu_{upd} signal is associated with unencapsulated Pt, then the difference between the H_{upd} and Cu_{upd} -derived ECSAs can be used to estimate the percentage of active Pt sites that have been successfully encapsulated by the CLD process. Applying these assumptions to the data in Figure 9, between 43 and 98% of the active Pt sites were covered with dense TiO₂ layers that block Cu²⁺, implying that between 2 and 57% of sites still remained exposed to the bulk electrolyte. The range of coverages estimated based on Cu_{upd} and H_{upd} -derived ECSAs is in line with the partial coverages of coatings seen in representative TEM/EELS images of the planar samples (Figures 4 and S8).

IV. CONCLUSIONS

Condensed layer deposition (CLD) is a promising method for encapsulating porous electrodes with nanoscopic coatings. TEM, EELS, and XPS measurements confirmed that platinized carbon foam (Pt/CF) electrodes could be successfully coated with TiO2 by using the CLD process. Hydrogen underpotential deposition (H_{upd}) and carbon monoxide stripping measurements showed that Pt sites encapsulated by CLD TiO₂ coatings remain active with minimal loss in electrochemically active surface area compared to bare Pt controls. Concurrently, these measurements revealed that H⁺ and CO molecules are able to transport through the overlayer and reach the TiO₂/Pt buried interface. Less positive onset and peak potentials were observed for TiO2/Pt electrodes during CO oxidation, indicating that the TiO₂/Pt active sites are characterized by altered binding environments compared to bare Pt sites exposed to the bulk electrolyte. In contrast to ECSAs derived from CO stripping measurements, the ECSAs of TiO₂/Pt determined from copper stripping voltammetry were substantially suppressed compared to H_{upd}-derived ECSAs, which was attributed to the ability of the TiO₂ coatings to block Cu²⁺ ions from reaching the active catalyst. Assuming the detected Cuund signal originates from exposed Pt, the difference between the Cu stripping and H_{upd} ECSAs was furthermore used to estimate the fraction of unencapsulated active Pt sites, which was found to be between 2 and 57%. Further optimization of the CLD process is necessary to minimize nonuniformities in coating coverage and thickness, which can lead to changes in local current densities, selectivity, and activity.

ASSOCIATED CONTENT

Supporting Information

The Supporting Information is available free of charge at https://pubs.acs.org/doi/10.1021/acsami.3c18366.

Electrode fabrication and BET characterization; image of samples prepared via FIB; SEM images; EDS maps; HAADF-STEM images; SAED pattern; EELS spectra;

annular bright and dark TEM images; XPS results and analysis; and images of coated samples (PDF)

AUTHOR INFORMATION

Corresponding Author

Daniel V. Esposito - Department of Chemical Engineering, Columbia Electrochemical Energy Center, and Lenfest Center for Sustainable Energy, Columbia University in the City of New York, New York, New York 10027, United States; orcid.org/0000-0002-0550-801X; Email: de2300@ columbia.edu

Authors

- Daniela V. Fraga Alvarez Department of Chemical Engineering, Columbia Electrochemical Energy Center, and Lenfest Center for Sustainable Energy, Columbia University in the City of New York, New York, New York 10027, United States; orcid.org/0000-0001-5127-427X
- Zhexi Lin Department of Chemical Engineering, Columbia Electrochemical Energy Center, and Lenfest Center for Sustainable Energy, Columbia University in the City of New York, New York, New York 10027, United States; orcid.org/0000-0002-6720-6922
- Zixiao Shi Department of Chemistry and Chemical Biology, Cornell University, Ithaca, New York 14853-0001, United States
- Amanda F. Baxter Department of Chemical Engineering, Columbia University in the City of New York, New York, New York 10027, United States
- Emily D. Wang Department of Chemical Engineering, Columbia University in the City of New York, New York, New York 10027, United States
- Dhruti Kuvar Department of Chemical Engineering, Columbia University in the City of New York, New York, New York 10027, United States
- Nafis Mahmud Gas Processing Center, Qatar University, Doha, Qatar
- Muftah H. El-Naas Gas Processing Center, Qatar University, Doha, Qatar; o orcid.org/0000-0002-6164-1421
- Héctor D. Abruña Department of Chemistry and Chemical Biology, Cornell University, Ithaca, New York 14853-0001, United States; oorcid.org/0000-0002-3948-356X
- David A. Muller School of Applied and Engineering Physics, Cornell University, Ithaca, New York 14853-0001, United States; orcid.org/0000-0003-4129-0473

Complete contact information is available at: https://pubs.acs.org/10.1021/acsami.3c18366

Notes

The authors declare no competing financial interest.

ACKNOWLEDGMENTS

D.V.E., D.V.F.A., M.H.E., and N.M. acknowledge the support of Qatar National Research Fund (a member of Qatar Foundation) through Grant # NPRP 12S-0215-190090. The findings achieved herein are solely the responsibility of the authors. D.V.E., D.V.F.A., M.H.E., and N.M. also acknowledge co-funding provided by Qatar Shell. Z.S., Dr. H.D.A., and Dr. D.A.M. were supported by the Center for Alkaline-Based Energy Solutions (CABES), part of the Energy Frontier Research Center (EFRC) program funded by the U.S. Department of Energy, under Grant DE-SC-0019445. Cornell Electron Microscopy Facilities were supported by the National Science Foundation (DMR-2039380, DMR-1719875). The authors acknowledge Dr. Phillippe Chow for his assistance with BET measurements, Dr. Amir Zangiabadi for his help with TEM measurements, and the use of facilities and instrumentation operated by the Columbia Nano Initiative. The authors thank Marshall Tekell (Columbia U.), Nicholas Mendez (Columbia U.), and Dr. Andrés Molina Villarino (Cornell U.) for helpful discussions and insights related to sample preparation and interpretation of characterization results.

REFERENCES

- (1) Mallapragada, D. S.; Dvorkin, Y.; Modestino, M. A.; Esposito, D. V.; Smith, W. A.; Hodge, B.-M.; Harold, M. P.; Donnelly, V. M.; Nuz, A.; Bloomquist, C.; Baker, K.; Grabow, L. C.; Yan, Y.; Rajput, N. N.; Hartman, R. L.; Biddinger, E. J.; Aydil, E. S.; Taylor, A. D. Decarbonization of the Chemical Industry through Electrification: Barriers and Opportunities. Joule 2023, 7 (1), 23-41.
- (2) Ramli, Z. A. C.; Kamarudin, S. K. Platinum-Based Catalysts on Various Carbon Supports and Conducting Polymers for Direct Methanol Fuel Cell Applications: A Review. Nanoscale Res. Lett. 2018, 13 (1), No. 410, DOI: 10.1186/s11671-018-2799-4.
- (3) Nabil, Y.; Cavaliere, S.; Harkness, I. A.; Sharman, J. D. B.; Jones, D. J.; Rozière, J. Novel Niobium Carbide/Carbon Porous Nanotube Electrocatalyst Supports for Proton Exchange Membrane Fuel Cell Cathodes. J. Power Sources 2017, 363, 20-26.
- (4) Liu, Z.; Ma, L.; Zhang, J.; Kitiya, H.; Hongsirikarn, K.; Goodwin, J. G. Pt Alloy Electrocatalysts for Proton Exchange Membrane Fuel Cells: A Review. Catal. Rev.: Sci. Eng. 2013, 55 (3), 255-288, DOI: 10.1080/01614940.2013.795455.
- (5) Monai, M.; Jenkinson, K.; Melcherts, A. E. M.; Louwen, J. N.; Irmak, E. A.; Van Aert, S.; Altantzis, T.; Vogt, C.; van der Stam, W.; Duchoň, T.; Šmíd, B.; Groeneveld, E.; Berben, P.; Bals, S.; Weckhuysen, B. M. Restructuring of Titanium Oxide Overlayers over Nickel Nanoparticles during Catalysis. Science 2023, 380 (6645),
- (6) Beatty, M. E. S.; Chen, H.; Labrador, N. Y.; Lee, B. J.; Esposito, D. V. Structure-Property Relationships Describing the Buried Interface between Silicon Oxide Overlayers and Electrocatalytic Platinum Thin Films. J. Mater. Chem. A 2018, 6, 22287-22300, DOI: 10.1039/c8ta06969g.
- (7) Robinson, J. E.; Labrador, N. Y.; Chen, H.; Sartor, B. E.; Esposito, D. V. Silicon Oxide-Encapsulated Platinum Thin Films as Highly Active Electrocatalysts for Carbon Monoxide and Methanol Oxidation. ACS Catal. 2018, 8 (12), 11423-11434.
- (8) Labrador, N. Y.; Songcuan, E. L.; De Silva, C.; Chen, H.; Kurdziel, S. J.; Ramachandran, R. K.; Detavernier, C.; Esposito, D. V. Hydrogen Evolution at the Buried Interface between Pt Thin Films and Silicon Oxide Nanomembranes. ACS Catal. 2018, 8 (3), 1767-
- (9) Esposito, D. V.; Guilimondi, V.; Vos, J. G.; Koper, M. T. M. Design Principles for Oxide-Encapsulated Electrocatalysts. In Ultrathin Oxide Layers for Solar and Electrocatalytic Systems; Frei, H.; Esposito, D., Eds.; The Royal Society of Chemistry, 2022; Chapter 7. (10) Bhardwaj, A. A.; Vos, J. G.; Beatty, M. E. S.; Baxter, A. F.; Koper, M. T. M.; Yip, N. Y.; Esposito, D. V. Ultrathin Silicon Oxide Overlayers Enable Selective Oxygen Evolution from Acidic and Unbuffered PH-Neutral Seawater. ACS Catal. 2021, 11 (3), 1316-
- (11) Beatty, M. E. S.; Gillette, E. I.; Haley, A. T.; Esposito, D. V. Controlling the Relative Fluxes of Protons and Oxygen to Electrocatalytic Buried Interfaces with Tunable Silicon Oxide Overlayers. ACS Appl. Energy Mater. 2020, 3 (12), 12338-12350.
- (12) Bau, J. A.; Takanabe, K. Ultrathin Microporous SiO₂ Membranes Photodeposited on Hydrogen Evolving Catalysts Enabling Overall Water Splitting. ACS Catal. 2017, 7 (11), 7931-7940.

- (13) Jo, W. J.; Katsoukis, G.; Frei, H. Ultrathin Amorphous Silica Membrane Enhances Proton Transfer across Solid-to-Solid Interfaces of Stacked Metal Oxide Nanolayers While Blocking Oxygen. *Adv. Funct. Mater.* **2020**, *30* (12), No. 1909262.
- (14) Buabthong, P.; Ifkovits, Z. P.; Kempler, P. A.; Chen, Y.; Nunez, P. D.; Brunschwig, B. S.; Papadantonakis, K. M.; Lewis, N. S. Failure Modes of Protection Layers Produced by Atomic Layer Deposition of Amorphous TiO₂ on GaAs Anodes. *Energy Environ. Sci.* **2020**, *13* (11), 4269–4279.
- (15) Onn, T. M.; Küngas, R.; Fornasiero, P.; Huang, K.; Gorte, R. J. Atomic Layer Deposition on Porous Materials: Problems with Conventional Approaches to Catalyst and Fuel Cell Electrode Preparation. *Inorganics* **2018**, *6* (1), No. 34, DOI: 10.3390/inorganics6010034.
- (16) Takenaka, S.; Arike, T.; Nakagawa, K.; Matsune, H.; Kishida, M.; Tanabe, E. Synthesis of Carbon Nanotube-Supported Pt Nanoparticles Covered with Silica Layers. *Carbon* **2008**, 46 (2), 365–368.
- (17) Takenaka, S.; Arike, T.; Matsune, H.; Tanabe, E.; Kishida, M. Preparation of Carbon Nanotube-Supported Metal Nanoparticles Coated with Silica Layers. *J. Catal.* **2008**, *257*, 345–355.
- (18) Park, K.; Goto, M.; So, M.; Takenaka, S.; Tsuge, Y.; Inoue, G. Influence of Cathode Catalyst Layer with SiO₂-Coated Pt/Ketjen Black Catalysts on Performance for Polymer Electrolyte Fuel Cells. *Catalysts* **2021**, *11* (12), No. 1517, DOI: 10.3390/catal11121517.
- (19) Takenaka, S.; Miyazaki, T.; Matsune, H.; Kishida, M. Highly Active and Durable Silica-Coated Pt Cathode Catalysts for Polymer Electrolyte Fuel Cells: Control of Micropore Structures in Silica Layers. Catal. Sci. Technol. 2015, 5 (2), 1133–1142.
- (20) Takenaka, S.; Miyamoto, H.; Utsunomiya, Y.; Matsune, H.; Kishida, M. Catalytic Activity of Highly Durable Pt/CNT Catalysts Covered with Hydrophobic Silica Layers for the Oxygen Reduction Reaction in PEFCs. *J. Phys. Chem. C* **2014**, *118*, 774–783, DOI: 10.1021/jp407928m.
- (21) Takenaka, S.; Goto, M.; Masuda, Y.; Emura, S.; Kishida, M. Improvement in the Durability of Carbon Black-Supported Pt Cathode Catalysts by Silica-Coating for Use in PEFCs. *Int. J. Hydrogen Energy* **2018**, 43 (15), 7473–7482.
- (22) Kobayashi, A.; Fujii, T.; Harada, C.; Yasumoto, E.; Takeda, K.; Kakinuma, K.; Uchida, M. Effect of Pt and Ionomer Distribution on Polymer Electrolyte Fuel Cell Performance and Durability. *ACS Appl. Energy Mater.* **2021**, *4* (3), 2307–2317.
- (23) Alink, R.; Singh, R.; Schneider, P.; Christmann, K.; Schall, J.; Keding, R.; Zamel, N. Full Parametric Study of the Influence of Ionomer Content, Catalyst Loading and Catalyst Type on Oxygen and Ion Transport in PEM Fuel Cell Catalyst Layers. *Molecules* 2020, 25 (7), No. 1523, DOI: 10.3390/molecules25071523.
- (24) Jasim, A. M.; He, X.; White, T. A.; Xing, Y. Nano-Layer Deposition of Metal Oxides via a Condensed Water Film. *Commun. Mater.* **2020**, *1* (1), No. 9, DOI: 10.1038/s43246-020-0010-9.
- (25) Jasim, A. M.; Al-Salihi, S.; Xing, Y. Communication—Platinum and Tin Oxide Dispersed in a Fluffy TiO₂ Nanolayer for Electrocatalytic Reduction of Oxygen. *J. Electrochem. Soc.* **2020**, *167* (11), No. 116526.
- (26) Al-Salihi, S.; Jasim, A. M.; Fidalgo, M. M.; Xing, Y. Removal of Congo Red Dyes from Aqueous Solutions by Porous γ -Alumina Nanoshells. *Chemosphere* **2022**, 286, No. 131769.
- (27) Jasim, A. M.; Xu, G.; Al-Salihi, S.; Xing, Y. Dense Niobium Oxide Coating on Carbon Black as a Support to Platinum Electrocatalyst for Oxygen Reduction. *ChemistrySelect* **2020**, 5 (37), 11431–11437
- (28) Xing, Y.; Jasmin, A. M. A Method of Forming Conformable Nanoscale Coatings on Substrates. W.O. Patent WO2019,140,169A1, 2019.
- (29) Liang, Y.; Sun, S.; Deng, T.; Ding, H.; Chen, W.; Chen, Y. The Preparation of TiO_2 Film by the Sol-Gel Method and Evaluation of Its Self-Cleaning Property. *Materials* **2018**, *11*, No. 450, DOI: 10.3390/ma11030450.

- (30) Xing, Y. Ultrathin Oxide Coatings Synthesized Via Wet Chemical Processes for Electrocatalytic Systems. In *Ultrathin Oxide Layers for Solar and Electrocatalytic Systems*; Frei, H.; Esposito, D., Eds.; The Royal Society of Chemistry, 2022.
- (31) Pourbaix, M. Titanium. In Atlas of Electrochemical Equilibria in Aqueous Solutions; NACE Foundation: Houston, 1974.
- (32) Fröschl, T.; Hörmann, U.; Kubiak, P.; Kucerová, G.; Pfanzelt, M.; Weiss, C. K.; Behm, R. J.; Hüsing, N.; Kaiser, U.; Landfester, K.; Wohlfahrt-Mehrens, M. High Surface Area Crystalline Titanium Dioxide: Potential and Limits in Electrochemical Energy Storage and Catalysis. *Chem. Soc. Rev.* **2012**, *41* (15), 5313–5360.
- (33) Gu, J.; Yan, Y.; Young, J. L.; Steirer, K. X.; Neale, N. R.; Turner, J. A. Water Reduction by a P-GaInP₂ Photoelectrode Stabilized by an Amorphous TiO₂ Coating and a Molecular Cobalt Catalyst. *Nat. Mater.* **2016**, *15* (4), 456–460.
- (34) Finke, C. E.; Omelchenko, S. T.; Jasper, J. T.; Lichterman, M. F.; Read, C. G.; Lewis, N. S.; Hoffmann, M. R. Enhancing the Activity of Oxygen-Evolution and Chlorine-Evolution Electrocatalysts by Atomic Layer Deposition of TiO₂. *Energy Environ. Sci.* **2019**, *12* (1), 358–365.
- (35) Xing, Y. Synthesis and Electrochemical Characterization of Uniformly-Dispersed High Loading Pt Nanoparticles on Sonochemically-Treated Carbon Nanotubes. *J. Phys. Chem. B* **2004**, *108* (50), 19255–19259.
- (36) Xing, Y.; Li, L.; Chusuei, C. C.; Hull, R. V. Sonochemical Oxidation of Multiwalled Carbon Nanotubes. *Langmuir* **2005**, *21* (9), 4185–4190.
- (37) van der Vliet, D. F.; Wang, C.; Li, D.; Paulikas, A. P.; Greeley, J.; Rankin, R. B.; Strmcnik, D.; Tripkovic, D.; Markovic, N. M.; Stamenkovic, V. R. Unique Electrochemical Adsorption Properties of Pt-Skin Surfaces. *Angew. Chem., Int. Ed.* **2012**, *51* (13), 3139–3142.
- (38) Jerkiewicz, G. Electrochemical Hydrogen Adsorption and Absorption. Part 1: Under-Potential Deposition of Hydrogen. *Electrocatalysis* **2010**, *1* (4), 179–199.
- (39) Carbon Foam | RVC Foam | Open Cell Foam | Reticulated Foamhttps. //ergaerospace.com/duocel-foam-surface-area/ (accessed July 13, 2022).
- (40) Cueva, P.; Hovden, R.; Mundy, J. A.; Xin, H. L.; Muller, D. A. Data Processing for Atomic Resolution Electron Energy Loss Spectroscopy. *Microsc. Microanal.* **2012**, *18* (4), 667–675.
- (41) Hatanaka, M.; Takahashi, N.; Takahashi, N.; Tanabe, T.; Nagai, Y.; Suda, A.; Shinjoh, H. Reversible Changes in the Pt Oxidation State and Nanostructure on a Ceria-Based Supported Pt. *J. Catal.* **2009**, *266* (2), 182–190.
- (42) Biesinger, M. C.; Lau, L. W. M.; Gerson, A. R.; Smart, R. S. C. Resolving Surface Chemical States in XPS Analysis of First Row Transition Metals, Oxides and Hydroxides: Sc, Ti, V, Cu and Zn. Appl. Surf. Sci. 2010, 257 (3), 887–898.
- (43) Landoulsi, J.; Genet, M. J.; Fleith, S.; Touré, Y.; Liascukiene, I.; Méthivier, C.; Rouxhet, P. G. Organic Adlayer on Inorganic Materials: XPS Analysis Selectivity to Cope with Adventitious Contamination. *Appl. Surf. Sci.* **2016**, 383, 71–83.
- (44) Green, C. L.; Kucernak, A. Determination of the Platinum and Ruthenium Surface Areas in Platinum–Ruthenium Alloy Electrocatalysts by Underpotential Deposition of Copper. I. Unsupported Catalysts. J. Phys. Chem. B 2002, 106 (5), 1036–1047.
- (45) Krylova, G.; Na, C. Photoinduced Crystallization and Activation of Amorphous Titanium Dioxide. *J. Phys. Chem. C* **2015**, 119 (22), 12400–12407.
- (46) Wang, L.; Li, W.; Zhang, M.; Tao, K. The Interactions between the NiB Amorphous Alloy and ${\rm TiO_2}$ Support in the NiB/TiO₂ Amorphous Catalysts. *Appl. Catal., A* **2004**, 259 (2), 185–190.
- (47) Stoyanov, E.; Langenhorst, F.; Steinle-Neumann, G. The Effect of Valence State and Site Geometry on Ti L3,2 and O K Electron Energy-Loss Spectra of Ti_xO_y Phases. *Am. Mineral.* **2007**, 92 (4), 577–586.
- (48) Burke, A. R.; Brown, C. R.; Bowling, W. C.; Glaub, J. E.; Kapsch, D.; Love, C. M.; Whitaker, R. B.; Moddeman, W. E. Ignition

- Mechanism of the Titanium-Boron Pyrotechnic Mixture. Surf. Interface Anal. 1988, 11 (6-7), 353-358.
- (49) Jerkiewicz, G.; Vatankhah, G.; Lessard, J.; Soriaga, M. P.; Park, Y. S. Surface-Oxide Growth at Platinum Electrodes in Aqueous H₂SO₄: Reexamination of Its Mechanism through Combined Cyclic-Voltammetry, Electrochemical Quartz-Crystal Nanobalance, and Auger Electron Spectroscopy Measurements. Electrochim. Acta 2004, 49 (9-10), 1451-1459.
- (50) Cohen, J. L.; Volpe, D. J.; Abruña, H. D. Electrochemical Determination of Activation Energies for Methanol Oxidation on Polycrystalline Platinum in Acidic and Alkaline Electrolytes. Phys. Chem. Chem. Phys. 2007, 9 (1), 49-77.
- (51) Attard, G. A.; Brew, A.; Hunter, K.; Sharman, J.; Wright, E. Specific Adsorption of Perchlorate Anions on Pt{hkl} Single Crystal Electrodes. Phys. Chem. Chem. Phys. 2014, 16 (27), 13689-13698.
- (52) Kamat, G. A.; Zeledón, J. A. Z.; Gunasooriya, G. T. K. K.; Dull, S. M.; Perryman, J. T.; Nørskov, J. K.; Stevens, M. B.; Jaramillo, T. F. Acid Anion Electrolyte Effects on Platinum for Oxygen and Hydrogen Electrocatalysis. Commun. Chem. 2022, 5 (1), No. 20, DOI: 10.1038/ s42004-022-00635-1.
- (53) Baruah, B.; Deb, P. Performance and Application of Carbon-Based Electrocatalysts in Direct Methanol Fuel Cell. Mater. Adv. **2021**, 2 (16), 5344-5364.
- (54) Solla-Gullón, J.; Vidal-Iglesias, F. J.; Herrero, E.; Feliu, J. M.; Aldaz, A. CO Monolayer Oxidation on Semi-Spherical and Preferentially Oriented (1 0 0) and (1 1 1) Platinum Nanoparticles. Electrochem. Commun. 2006, 8 (1), 189-194.
- (55) García, G.; Koper, M. T. M. Carbon Monoxide Oxidation on Pt Single Crystal Electrodes: Understanding the Catalysis for Low Temperature Fuel Cells. ChemPhysChem 2011, 12 (11), 2064-2072.
- (56) Mcpherson, I. J.; Ash, P. A.; Jones, L.; Varambhia, A.; Jacobs, R. M. J.; Vincent, K. A. Electrochemical CO Oxidation at Platinum on Carbon Studied through Analysis of Anomalous in Situ IR Spectra. J. Phys. Chem. C 2017, 121, 17176-17187, DOI: 10.1021/ acs.jpcc.7b02166.
- (57) Ciapina, E. G.; Santos, S. F.; Gonzalez, E. R. Electrochemical CO Stripping on Nanosized Pt Surfaces in Acid Media: A Review on the Issue of Peak Multiplicity. J. Electroanal. Chem. 2018, 815, 47-60.
- (58) Ciapina, E. G.; Santos, S. F.; Gonzalez, E. R. The Electro-Oxidation of Carbon Monoxide and Ethanol on Supported Pt Nanoparticles: The Influence of the Support and Catalyst Microstructure. J. Solid State Electrochem. 2013, 17 (7), 1831-1842.
- (59) Qin, Y. H.; Li, Y.; Lv, R. L.; Wang, T. L.; Wang, W. G.; Wang, C. W. Enhanced Methanol Oxidation Activity and Stability of Pt Particles Anchored on Carbon-Doped TiO₂ Nanocoating Support. J. Power Sources 2015, 278, 639-644.
- (60) Guo, X.; Guo, D. J.; Qiu, X. P.; Chen, L. Q.; Zhu, W. T. Excellent Dispersion and Electrocatalytic Properties of Pt Nanoparticles Supported on Novel Porous Anatase TiO2 Nanorods. J. Power Sources 2009, 194 (1), 281-285.
- (61) Chen, J. M.; Sarma, L. S.; Chen, C. H.; Cheng, M. Y.; Shih, S. C.; Wang, G. R.; Liu, D. G.; Lee, J. F.; Tang, M. T.; Hwang, B. J. Multi-Scale Dispersion in Fuel Cell Anode Catalysts: Role of TiO2 towards Achieving Nanostructured Materials. J. Power Sources 2006, 159, 29-33.
- (62) Dey, S.; Dhal, G. C. Property and Structure of Various Platinum Catalysts for Low-Temperature Carbon Monoxide Oxidations. Mater. Today Chem. 2020, 16, No. 100228.
- (63) Zhang, Z.; Liu, J.; Gu, J.; Su, L.; Cheng, L. An Overview of Metal Oxide Materials as Electrocatalysts and Supports for Polymer Electrolyte Fuel Cells. Energy Environ. Sci. 2014, 7 (8), 2535-2558.
- (64) Hepel, M.; Dela, I.; Hepel, T.; Luo, J.; Zhong, C. J. Novel Dynamic Effects in Electrocatalysis of Methanol Oxidation on Supported Nanoporous TiO₂ Bimetallic Nanocatalysts. Electrochim. Acta 2007, 52 (18), 5529-5547.
- (65) Torres, P. A. L.; El-Sayed, H. A.; Schwämmlein, J. N.; Friedrich, F.; Gasteiger, H. A. Hydrogen Gas Promoted Self-Limiting Copper Monolayer Deposition on Platinum. J. Electrochem. Soc. 2021, 168 (5), No. 052508, DOI: 10.1149/1945-7111/abfe79.

- (66) Vukmirovic, M. B.; Bliznakov, S. T.; Sasaki, K.; Wang, J. X.; Adzic, R. R. Electrodeposition of Metals in Catalyst Synthesis: The Case of Platinum Monolayer Electrocatalysts. Electrochem. Soc. Interface 2011, 20 (2), No. 33, DOI: 10.1149/2.F04112if.
- (67) Makivić, N.; Cho, J.-Y.; Harris, K. D.; Tarascon, J.-M.; Limoges, B.; Balland, V. Evidence of Bulk Proton Insertion in Nanostructured Anatase and Amorphous TiO₂ Electrodes. Chem. Mater. 2021, 33 (9), 3436-3448.
- (68) Röttcher, N. C.; Ku, N. P.; Minichova, M.; Ehelebe, K.; Cherevko, S. Comparison of Methods to Determine Electrocatalysts' Surface Area in Gas Diffusion Electrode Setups: A Case Study on Pt/ C and PtRu/C. J. Phys. Energy 2023, 5, No. 024007, DOI: 10.1088/ 2515-7655/acbe1b.